Finite size effects in critical fiber networks†

Sadjad Arzash, [ab] Jordan L. Shivers [ab] and Fred C. MacKintosh *[abc]

Fibrous networks such as collagen are common in physiological systems. One important function of these networks is to provide mechanical stability for cells and tissues. At physiological levels of connectivity, such networks would be mechanically unstable with only central-force interactions. While networks can be stabilized by bending interactions, it has also been shown that they exhibit a critical transition from floppy to rigid as a function of applied strain. Beyond a certain strain threshold, it is predicted that underconstrained networks with only central-force interactions exhibit a discontinuity in the shear modulus. We study the finite-size scaling behavior of this transition and identify both the mechanical discontinuity and critical exponents in the thermodynamic limit. We find both non-mean-field behavior and evidence for a hyperscaling relation for the critical exponents, for which the network stiffness is analogous to the heat capacity for thermal phase transitions. Further evidence for this is also found in the self-averaging properties of fiber networks.

1 Introduction

In addition to common thermal phase transitions such as melting or ferromagnetism, there are a number of athermal phase transitions such as rigidity percolation[1–3] and zero-temperature jamming.[4–8] These athermal transitions may even exhibit signatures of criticality that are similar to thermal systems. In the case of rigidity percolation, as bond probability or average connectivity z increases on a random central-force network, the number of floppy modes decreases by adding constraints until the isostatic connectivity z_c is reached, at which the system becomes rigid. A simple counting argument by Maxwell shows that $z_c \approx 2d$ where d is dimensionality.[9,10] This linear rigidity transition has been studied in random network models with additional bending interactions.[11–13] In general, floppy subisostatic central force networks can be stabilized by various mechanisms or additional interactions such as extra springs,[14] bending resistance,[15] thermal fluctuations,[16,17] and applied strain.[18,19] Sharma *et al.*[20] recently showed that networks with $z < z_c$ exhibit a line of critical floppy-to-rigid transitions under shear deformation and that this line of mechanical phase transitions can account for the nonlinear rheology of collagen networks. The corresponding phase diagram is schematically shown in Fig. 1, where the critical strain γ_c at the transition is a function of connectivity $z < z_c$.
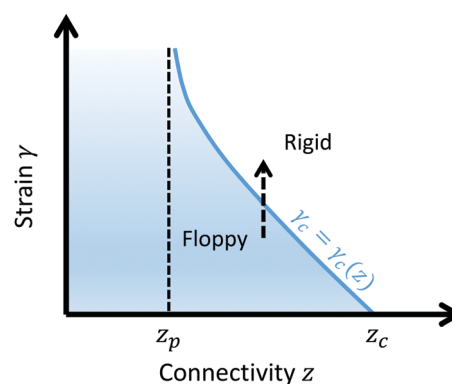
[a] Department of Chemical & Biomolecular Engineering, Rice University, Houston, TX 77005, USA. E-mail: fcmack@gmail.com

[b] Center for Theoretical Biological Physics, Rice University, Houston, TX 77030, USA

[c] Departments of Chemistry and Physics & Astronomy, Rice University, Houston, TX 77005, USA

† Electronic supplementary information (ESI) available. See DOI: 10.1039/d0sm00764a

Fig. 1 Rigidity phase diagram of central force networks. Upon increasing the average connectivity z at $\gamma = 0$, a network passes through three distinct regimes: (i) a disconnected structure for connectivity less than the percolation connectivity $z < z_p$ (ii) a percolated but floppy network for $z_p < z < z_c \simeq 2d$ and (iii) a rigid network for connectivity greater than z_c. Applying a sufficiently large finite strain to an otherwise floppy network with $z_p < z < z_c$ rigidifies the system. For a given z in this range, a critical transition is observed with increasing strain, as indicated by the dashed arrow. The second-order line of transitions is characterized by a critical strain $\gamma_c(z)$ that varies linearly with z near z_c[14] (see also Fig. S3, ESI†).

Recent experiments[21–24] have shown that collagen biopolymers form networks that are in the subisostatic regime with $z < z_c$. It has also been shown that the rheology of such networks is consistent with computational fiber network models that include both strong stretching interactions and weak fiber bending rigidity.[20,22] Although even a weak bending rigidity tends to suppress the critical signatures of the transition shown in Fig. 1, the critical exponents can still be identified both theoretically and experimentally in a way similar, *e.g.*, to

Paper

Soft Matter

ferromagnetism at non-zero applied field. To understand criticality and finite-size effects in the strain-controlled transition, we focus on fiber networks with purely central force interactions as a function of shear strain γ. At a critical strain γ_c, there can be a small but finite discontinuity in the differential shear modulus $K = \partial\sigma/\partial\gamma$, where σ is the shear stress.[25,26] Fig. 2 shows the macroscopic modulus, shear stress and elastic energy of a diluted triangular network as a function of the distance above its critical strain. Although both elastic energy E and shear stress σ approach zero as $\Delta\gamma = \gamma - \gamma_c$ approaches zero from above, the stiffness K exhibits a finite discontinuity K_c. The left inset of Fig. 2 shows K versus $|\Delta\gamma|^f$, where $f \neq 1$ is a non-mean-field scaling exponent. The observed straight line in this linear plot illustrates the critical scaling behavior of K near γ_c. Moreover, a distinct discontinuity in the modulus can be seen in the right inset of Fig. 2, showing the region closer to γ_c. The scaling behavior of K and the critical exponent f are more systematically studied in the later sections, where we study the finite-size scaling of the discontinuity and its effect on the scaling exponents, which have also previously been studied using a complementary approach with the addition of small, non-zero bending rigidity.[20] Using these modified exponents, we test scaling relations recently predicted for fiber networks.[27]

2 Simulation method

To investigate the stiffness discontinuity in fiber networks, we use various network models including (i) triangular, (ii) phantomized triangular,[15,22] (iii) 2D and (iv) 3D jammed-packing-derived,[14,26,28–30] (v) Mikado,[31,32] and (vi) 2D Voronoi network.[33,34] Triangular networks are built by depositing individual fibers of length W on a periodic triangular lattice. The lattice spacing is $\ell_0 = 1$. A full triangular network has an average
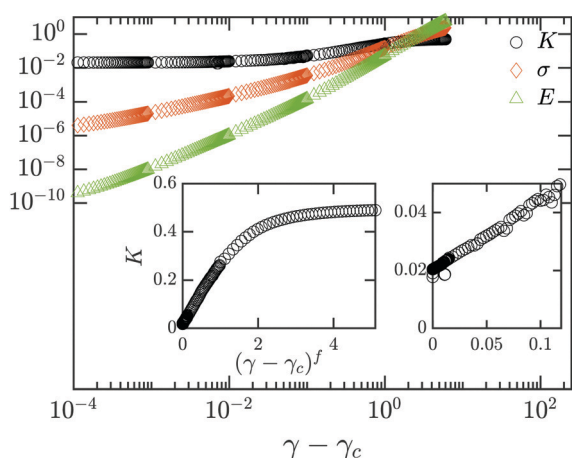
Fig. 2 Elastic energy E, shear stress σ, and differential shear modulus K versus excess shear strain to the critical point $\gamma - \gamma_c$ for a single realization of a subisostatic triangular network with $z = 3.3$. We use the finite modulus at the critical strain γ_c as the shear modulus discontinuity, i.e., $K_c = K(\gamma_c)$. Inset: A linear plot showing the scaling behavior of K for the same sample. By zooming in this plot on the right side, we observe a distinct modulus discontinuity K_c.

connectivity of $z = 6$. In order to avoid the trivial effects of system-spanning fibers, we initially cut a single random bond from every fiber. Since the number of connections for a cross-link in real biopolymer networks is either 3 (branching point) or 4 (fiber crossing), we enforce this local connectivity in phantomized triangular model. A single node in a full triangular network has three crossing fibers. We phantomize the network by detaching one of these fibers randomly for every node.[22,35] Therefore, a fully phantomized triangular network has an average connectivity of $z = 4$. Similar to the triangular network model, a random bond is removed from every fiber to avoid system-spanning fibers.

We note that our lattice models are not generic, i.e., the nodes are not displaced from an initial regular lattice. Although generic lattices can be important for linear elasticity,[3,36] the nonlinear elasticity studied here is insensitive to small displacements in the initial configuration, as shown in ref. 37. This is due to the fact that the transition we study occurs at a finite strain threshold, by which significant nonaffine deformation has occurred. 2D (3D) packing-derived networks are generated by randomly placing $N = W^2 (W^3)$ disks (spheres) in a periodic box (cube) of length W. We use 50/50 bidisperse particle mixture with radii ratio of 1.4. These frictionless particles interact via a harmonic soft repulsive potential.[38–40] The particles are uniformly expanded until the system exhibits both non-zero bulk and shear moduli, i.e., the system is jammed at which a contact network excluding rattlers is derived. This contact network shows an average connectivity of $z \simeq z_c$. Mikado networks are constructed by populating a box of size W with N fibers of length L. Permanent crosslinks are introduced at the crossing points between two fibers. Because of the preparation procedure for the Mikado model, the average connectivity of the network approaches 4 from below as number of fibers N increases. To construct Mikado networks, we choose a line density of $NL^2/W^2 \simeq 7$ that results in an average connectivity of $z \simeq 3.4$. The 2D Voronoi model is prepared by performing a Voronoi tessellation of $W^2/2$ random seeds in a periodic box with side length of W, using the CGAL library.[41] A full Voronoi network has an average connectivity of $z = 3$.

For all network models, we randomly cut bonds until the desired average connectivity $z < z_c$ is reached. Any remaining dangling bonds are removed since they do not contribute to the network's stiffness. The random dilution process not only yields a subisostatic network similar to real biopolymers but also introduces disorder in the system. All crosslinks in our computational models are permanent and freely hinged. An example image of each model is shown in Fig. S1 in ESI.† Among these computational models, we note that the bond length distribution of Mikado and Voronoi models is similar to the observed filament length distribution of collagen networks.[21]

In the above models, the bonds are treated as simple Hookean springs. Therefore, the elastic energy of the network is calculated as

$$E = \frac{\mu}{2} \sum_{ij} \frac{\left(\ell_{ij} - \ell_{ij,0}\right)^2}{\ell_{ij,0}}, \tag{1}$$

in which μ (in units of energy/length) is the stretching (Young's) modulus of individual bonds, ℓ_{ij} and $\ell_{ij,0}$ are the current and rest bond length between nodes i and j respectively. We note that the rest lengths are defined as bond lengths after constructing the networks, *i.e.*, prior to any deformation. The sum is taken over all bonds in the network. We set $\mu = 1$ in our simulations.

We apply simple volume-preserving shear deformations in a step-wise procedure with small step size. The deformation tensors in 2D and 3D are as follow

$$\Lambda_{2D}(\gamma) = \begin{bmatrix} 1 & \gamma \\ 0 & 1 \end{bmatrix}, \quad \Lambda_{3D}(\gamma) = \begin{bmatrix} 1 & 0 & \gamma \\ 0 & 1 & 0 \\ 0 & 0 & 1 \end{bmatrix} \quad (2)$$

where γ is the shear strain and the networks are sheared in x-direction. Note that the 3D networks are deformed in x–z plane.

We assume a quasi-static process, *i.e.*, the system reaches mechanical equilibrium after each deformation step. Therefore, after each strain step, we minimize the elastic energy in eqn (1) using one of the multidimensional minimization algorithms such as FIRE,[42] conjugate gradient,[43] and BFGS2 method from the GSL library.[44] To reduce finite size effects, we utilize periodic boundary conditions in both directions. Moreover, we use Lees–Edwards boundary conditions to deform the networks.[45] After finding the mechanical equilibrium configuration at each strain step, we compute the stress components as follows[27]

$$\sigma_{\alpha\beta} = \frac{1}{2V} \sum_{ij} f_{ij,\alpha} r_{ij,\beta}, \quad (3)$$

in which V is the volume of simulation box, $f_{ij,\alpha}$ is the α component of the force exerted on node i by node j, and $r_{ij,\beta}$ is the β component of the displacement vector connecting nodes i and j. The differential shear modulus K is calculated as $K = d\sigma_{xy}/d\gamma$ in 2D and $K = d\sigma_{xz}/d\gamma$ in 3D at each strain value. To remove any possible asymmetry in K, we shear each realization in both positive and negative shear strains. Unless otherwise stated, in order to obtain reliable ensemble averages, we use at least 100 different realizations for every network model.

3 Results

By applying shear strain, the subisostatic networks with central force interactions undergo a mechanical phase transition from a floppy to a rigid state.[20,46] In contrast to percolation- or jamming-like transitions in which the system rigidifies due to increasing number of bonds or contacts, fiber network models have static structures. Therefore, this floppy-to-rigid transition occurs because of the emergence of finite tension under deformation, here shear strain. The transition point is a function of network's geometry as well as network's connectivity z (see the schematic phase diagram in Fig. 1). As shown in Fig. 3, a branch-like tensional structure appears at the critical strain that is responsible for the network's rigidity. This rigidity mechanism can be understood in terms of the percolation of
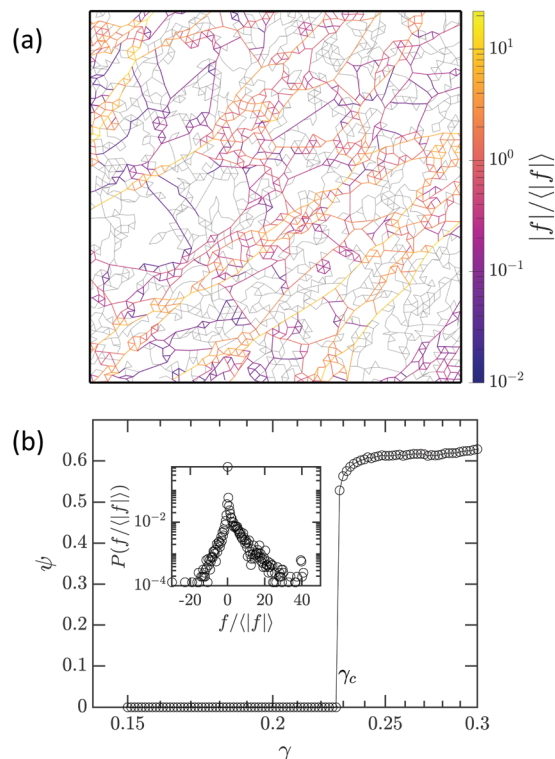

Fig. 3 (a) A small section of a triangular network with connectivity $z = 3.3$ at the critical strain $\gamma = \gamma_c$. The gray bonds are those with zero force. Bonds with larger forces have a brighter color. This branch–like force chain that appears at the critical strain rigidifies the otherwise floppy network. (b) The participation ratio ψ, the ratio of bonds under a finite force to all present bonds, *versus* shear strain γ for the network in (a). As shown, a large portion of bonds undergoes a finite force at the critical strain, *i.e.*, $\psi_c \simeq 0.5$. Inset: The force distributions of the network in (a) at the critical strain, where $\langle|f|\rangle$ is the average of absolute values of bond forces.

these tensional paths. By computing the participation ratio ψ as the ratio of bonds with non-zero force to all present bonds in the network, we find that a large portion of the network is under a finite force at the transition point (see Fig. 3b). To calculate ψ we use the absolute value of bond forces $|f_{ij}|$, where $f_{ij} > 0$ corresponds to tension. The force distribution at the critical strain is shown in the inset of Fig. 3b. The behavior of this distribution is similar to (compressive) contact force distributions in particle packings.[38,39,47–49] Here, however, the distribution shows that there are more tensile than compressive forces at the critical strain, which stabilize the network. Consistent with prior work,[30] we find that the force distribution decays exponentially at the critical strain.

To further understand this criticality in central force networks, we investigate the moments of force distribution that are defined as

$$M_k = \left\langle \frac{1}{N_b} \sum_{ij} |f_{ij}|^k \right\rangle, \quad (4)$$

in which the angle brackets represent the ensemble average over random realizations, N_b is the number of all bonds, and $|f_{ij}| = |\mu(\ell_{ij} - \ell_{ij,0})/\ell_{ij,0}|$ is the magnitude of force on bond ij.

Similar to the behavior of percolation on elastic networks,[13,50–52] we find that the moments M_k obey a scaling law near the critical strain

$$M_k \sim |\gamma - \gamma_c|^{q_k}. \tag{5}$$

This scaling behavior of the first three moments is shown in Fig. S4 in ESI.† For a triangular network with $z = 3.3$, we find that $q_1 = 1.3 \pm 0.1$, $q_2 = 2.5 \pm 0.1$ and $q_3 = 3.7 \pm 0.1$. Interestingly, we observe that $q_k \simeq q_{k-1} + 1$ for $k > 1$. Note that the zeroth moment of the force distribution is the participation ratio ψ shown in Fig. 3b. The mass fraction of the tensional backbone that appears at the critical strain is given by the participation ratio or zeroth moment at γ_c.[51,53] In plotting the mass of the tensional structure at the critical strain *versus* system size W, we find that the fractal dimension of this backbone appears to be the same as the Euclidean dimension of 2 (see Fig. S8 in ESI†).

Of particular interest are the macroscopic properties of fiber networks such as stiffness K near the transition. As we approach the critical point, we find that K shows a finite discontinuity K_c, in agreement with prior work.[25,26] Fig. 2 shows the behavior of one random realization of a diluted triangular network very close to its critical strain $\gamma - \gamma_c \simeq 10^{-4}$. In order to find the sample-specific critical point $\gamma_c(W,i)$ for a network with size W, we use the bisection method.[26] By performing an initial step-wise shearing simulation for every random sample, we first find a strain value $\gamma_{R,i}$ at which the network becomes rigid, *i.e.*, the shear stress calculated from eqn (3) reaches a threshold value. Here we use 10^{-9} for the stress threshold. Our results, however, are insensitive to the choice of the threshold value as long as we use a sufficiently small value. The prior strain value to $\gamma_{R,i}$ is considered as the nearest floppy point $\gamma_{F,i}$. Modifying the bracket $[\gamma_{F,i}, \gamma_{R,i}]$ in at least 20 bisection steps, we are able to accurately identify the critical point for every random sample i. After identifying the critical point, the network is sheared in a step-wise manner from $\gamma_c(W,i)$. Therefore, the final ensemble averages of a specific system size are taken over random realizations with the same distance from their critical strain. Prior work has established that this is a suitable averaging method for finite systems with large disorder.[54]

As shown previously[25] for purely central-force networks, the stiffness K exhibits a scaling behavior with the excess shear strain

$$K - K_c \sim |\gamma - \gamma_c|^f, \tag{6}$$

in which K_c represents a discontinuity in the shear modulus at the transition and f is a non-mean-field exponent. Subisostatic networks with central force interactions are floppy below this transition. In order to understand the behavior of networks in $\gamma < \gamma_c$ regime, we introduce an additional bending rigidity.[15,22,27] In the presence of a weak bending rigidity κ, the floppy-to-rigid transition in networks becomes a crossover between bend-dominated and stretch-dominated regimes.[20,27,46,55] In the small strain regime $\gamma < \gamma_c$, the shear modulus is proportional to the bending rigidity κ and the following scaling form captures the behavior of K for bend-stabilized fiber networks[20]
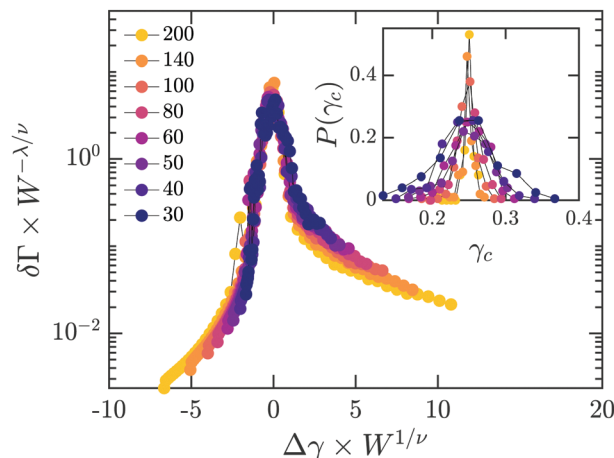

Fig. 4 The finite-size collapse of nonaffine fluctuations according to eqn (9). The data are obtained for triangular networks with $z = 3.3$ and different lateral size W as specified in the legend. Inset: Shows distributions of the critical strain for the same networks.

$$K \approx |\gamma - \gamma_c|^f \mathscr{G}_\pm(\kappa/|\gamma - \gamma_c|^\phi), \tag{7}$$

in which ϕ is a scaling exponent and $\mathscr{G}_\pm$ is the scaling function for regimes above and below the critical strain. In later sections, we discuss in detail the procedure of finding these scaling exponents f and ϕ.

With the scaling exponents f and ϕ obtained, we repeat the tests previously carried out for the scaling theory in ref. 27. Specifically, we consider the finite-size scaling of the nonaffine fluctuations of a diluted triangular network in Fig. 4. The nonaffine displacements are measured by the differential non-affinity parameter defined as

$$\delta\Gamma = \frac{\langle \|\delta \mathbf{u}^{NA}\|^2 \rangle}{\ell^2 \delta\gamma^2}, \tag{8}$$

in which ℓ is the typical bond length of the network, and $\delta \mathbf{u}^{NA} = \mathbf{u} - \mathbf{u}^{affine}$ is the nonaffine displacement of a node that is caused by applying an infinitesimal shear strain $\delta\gamma$. To better illustrate this parameter, we show the nonaffine displacement vectors of nodes for a diluted triangular network before, at and after the critical strain in Fig. S5 in ESI.†[46] The differential nonaffinity $\delta\Gamma$ diverges at the critical strain for central force networks, with a susceptibility-like exponent $\lambda = \phi - f$, *i.e.*, $\delta\Gamma \sim |\Delta\gamma|^{-\lambda}$.[27,46,56] Moreover, as the system approaches the critical strain, the correlation length diverges as $\xi \sim |\Delta\gamma|^{-\nu}$. When the correlation length is smaller than the system size W, *i.e.*, $|\Delta\gamma| \times W^{1/\nu} > 1$, we should find $\delta\Gamma \sim |\Delta\gamma|^{-\lambda}$. Near the critical strain, however, the finite-size effects result in $\delta\Gamma \sim |\Delta\gamma|^{\lambda/\nu}$. Therefore, the following scaling form must capture the behavior of fluctuations[46]

$$\delta\Gamma = W^{\lambda/\nu} \mathscr{H}(\Delta\gamma W^{1/\nu}), \tag{9}$$

where the scaling function (x) is constant for $|x| < 1$ and $|x|^{-\lambda}$ otherwise. The differential nonaffinity is shown for different system sizes of a diluted triangular network in Fig. S5 in ESI.† Based on the above scaling form, we perform a finite-size

scaling analysis as shown in Fig. 4. The correlation length exponent ν is computed from the hyperscaling relation $f = d\nu - 2$ obtained for this transition in prior work,[27] using the exponent f that is computed by considering the stiffness discontinuity. This excellent collapse of fluctuations further emphasizes the true critical nature of the transition as well as consistency with the hyperscaling relation $f = d\nu - 2$ in fiber networks, even accounting for the discontinuity in K. As noted before, this discontinuity has no bearing on the order of the transition, since K is not the order parameter, and is more analogous to the heat capacity in a thermal phase transition.[27] The inset of Fig. 4 shows the distribution of critical strains for the same networks in the main figure. As system size increases, the critical strain distribution becomes narrower. Although we focus on finite-size effects in computational fiber models primarily in order to properly identify the behavior of such networks in the thermodynamic limit, we note that experimental rheology on physical collagen networks can also be strongly affected by the sample size, e.g., in sample size dependence of the yield strain.[57] This is likely due to the rather large mesh size of order 10 μm in many of the experimental studies.

As indicated above, the exponent f is analogous to the heat capacity exponent α in thermal critical phenomena, but with opposite sign. Based on the Harris criterion,[58] a positive $f > 0$ (i.e., $\alpha < 0$), for which $\nu > 2/d$, implies that weak randomness does not change the behavior of critical fiber networks. Closely related to the Harris criterion is the self-averaging property in critical phenomena. Any observable $X = E$, σ or K has different values for different random samples. Therefore for a system with size W, we can define for observable X a probability distribution function $P(X,W)$, which is characterized by its average $\langle X \rangle$ and variance $V(X) = \langle X^2 \rangle - \langle X \rangle^2$. A system is self-averaging if the relative variance $R_V(X) = V(X)/\langle X \rangle^2 \to 0$ as $W \to \infty$. In other words, the ensemble average of a self-averaging system does not depend on the disorder introduced by random samples as the system size becomes infinite.

Far from the transition, where the system size W is much larger than the correlation length ξ, the Brout argument,[59] which is based on the central limit theorem, indicates strong self-averaging $R_V(X) \sim W^{-d}$ where d is dimensionality.[60] Indeed, for our 2D fiber networks away from the critical strain, we find that the relative variance of macroscopic properties decreases with system size as W^{-2}, i.e., fiber networks exhibit strong self-averaging off criticality (see Fig. 5b). Near the transition, however, the correlation length becomes larger than the system size $W \ll \xi$ and the Brout argument does not hold. Therefore, at criticality there is no reason to expect $R_V(X) \sim W^{-d}$.[60-62] For example, it is established that $R_V(X)$ shows a W-independent behavior, i.e., no self-averaging at the percolation transition for the mass of spanning cluster[63] and the conductance of diluted resistor networks.[64] A weak self-averaging, that corresponds to $R_V(X) \sim W^{-a}$ with $0 < a < d$, has been identified in bond-diluted Ashkin–Teller models.[60] As proved by Aharony and Harris,[61] when randomness is irrelevant, i.e., $\nu > 2/d$ the system exhibits a weak self-averaging behavior where $R_X \sim W^{\alpha/\nu}$ (in our fiber networks $R_X \sim W^{-f/\nu}$).
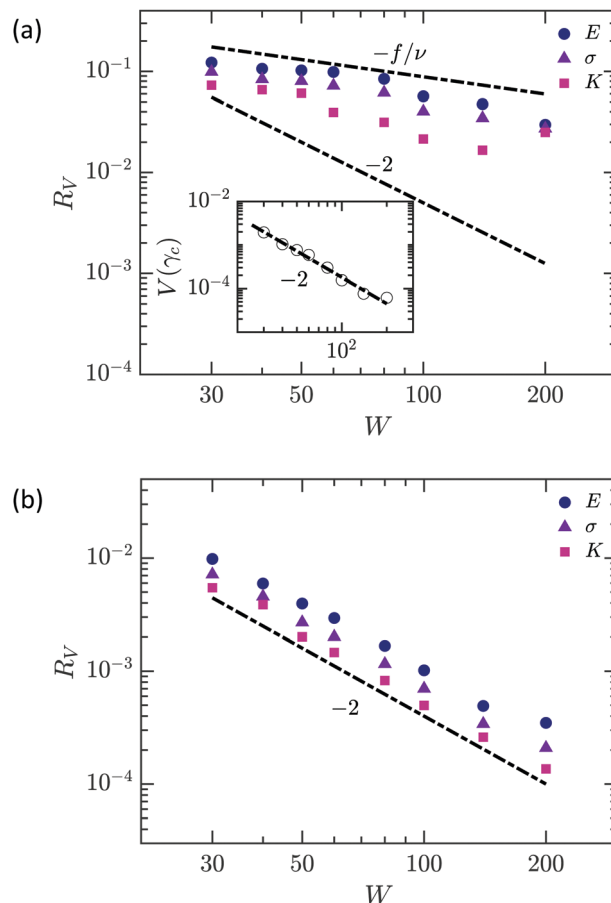

Fig. 5 (a) The relative variance of different quantities specified in the legend at the critical strain for a triangular network with $z = 3.3$ versus linear system size W. Inset: The scaling behavior of variance of critical strains versus system size for the same model. (b) The relative variance of the macroscopic quantities as specified in the legend for the same model in (a) away from the critical strain versus linear system size W.

As shown in Fig. 5a, fiber networks appear to exhibit a weak self-averaging at the critical strain, with an exponent close to f/ν. We note that $R_V(X)$ in Fig. 5a is computed in the regime where $|\Delta\gamma| \times W^{1/\nu} \approx 1$. We also find that the variance of critical strains decreases as $V(\gamma_c) \sim W^{-2}$ (see the inset of Fig. 5a), in accordance with Aharony and Harris prediction.[61]

As prior work showed,[14,26] the shear modulus discontinuity K_c vanishes as network connectivity z approaches the isostatic threshold $z_c = 2d$. Fig. 6 shows the behavior of K_c versus network connectivity z. As expected, K_c decreases as z approaches z_c. Moreover, as z decreases towards the connectivity percolation transition for a randomly diluted triangular network, we observe a decreasing trend in K_c. This regime can be explained by plotting the participation ratio at the critical strain ψ_c in the inset of Fig. 6. As we see ψ_c has a small value for networks with z close to the percolation connectivity. These small tensional patterns are responsible for the network's rigidity at critical strain, hence resulting in lower modulus discontinuity K_c.

In order to understand the network behavior in the thermodynamic limit, we study the finite-size effects in more detail.
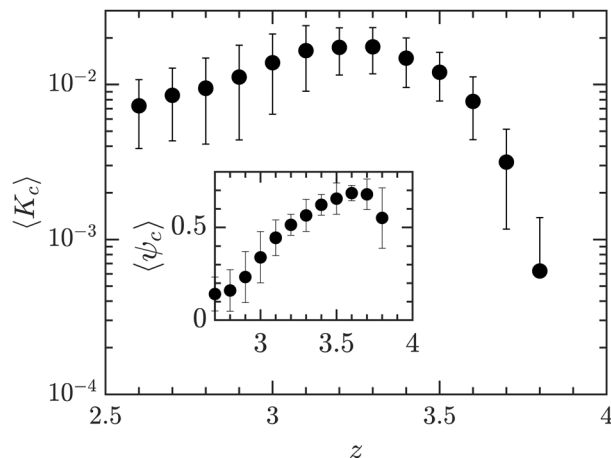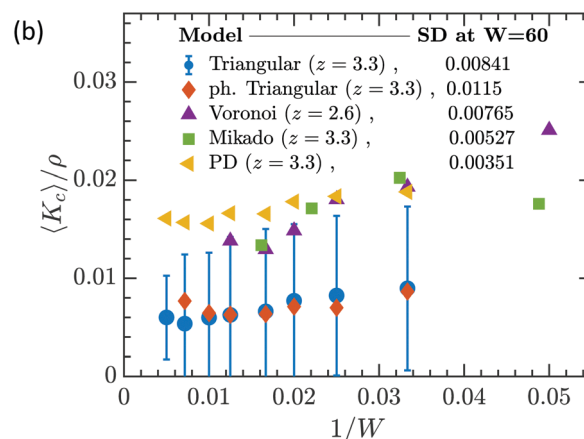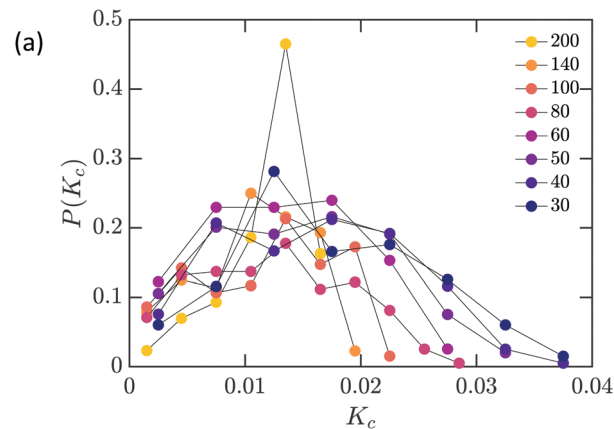
Fig. 6 Shear modulus discontinuity *versus* connectivity z for a triangular network. As connectivity z approaches the isostatic point z_c, the jump in shear modulus vanishes $K_c \rightarrow 0$. On the other hand, for networks with low connectivity, a small tensional pattern is responsible for the rigidity of the system. Therefore, K_c decreases as z decreases towards the percolation connectivity. Inset: Participation ratio at the critical strain *versus* connectivity z.

One trivial finite-size effect is observed by studying the participation ratio ψ. For small number of random realizations, a strand-like percolated force chain, which appears at the critical strain, continues to bear tensions under deformation. This effect results in a plateau in network stiffness K, as shown in Fig. S7 in ESI.† This plateau effect is more prevalent in network models with long, straight fibers such as the triangular model. We next explore the finite-size effects of stiffness discontinuity in fiber networks. The distributions of K_c for various system size are shown in Fig. 7a. The mean of these distributions *versus* inverse system size exhibits a slow decreasing trend for all different network models (Fig. 7b). However, we find that this discontinuity remains finite but small (of order 0.01) for all network models as we approach the thermodynamic limit $1/W \rightarrow 0$, consistent with findings of ref. 25 for the Mikado model. This is similar to the behavior of the linear bulk modulus for sphere packings at the jamming transition, which exhibits a finite discontinuity in z in the thermodynamic limit.[36,48,65,66] Vermeulen *et al.*[25] argued that the nonlinear shear modulus discontinuity in fiber networks is due to an emerging single state of self-stress at the network's critical strain. Consistent with this, we find a non-fractal stress backbone at the critical strain.

As mentioned above, the stiffness exponent f has a non-mean-field value, *i.e.*, $f \neq 1$. In fiber networks, the correlation length scales as $\xi \sim \Delta\gamma^{-\nu}$. True critical behavior in simulation results such as ours should only be apparent when the correlation length remains smaller than the system size, *i.e.*, $|\Delta\gamma| \times W^{1/\nu} > 1$.[20,27] Near the critical point, however, the correlation length diverges and the stiffness scales as $K - K_c \sim W^{-f/\nu}$. Therefore, the following scaling function captures the stiffness behavior

$$K - K_c = W^{-f/\nu}\mathscr{F}(\Delta\gamma W^{1/\nu}), \qquad (10)$$


Fig. 7 (a) The distributions of shear modulus discontinuity K_c for triangular networks with $z = 3.3$ and different system sizes as specified in the legend. (b) Shear modulus discontinuity K_c *versus* inverse system size $1/W$, for various 2D network models as specified in the legend (for Mikado model we used square root of present nodes in the network as W). The data are normalized with the length density ρ for every model. The standard deviations are only shown for the triangular network, though the standard deviation at $W = 60$ for every model is shown in the legend.

in which the function $\mathscr{F}(x)$ is a constant for $x < 1$ and x^f for $x > 1$. Note that we are only able to investigate one side of the transition $\Delta\gamma > 0$ for central force networks.
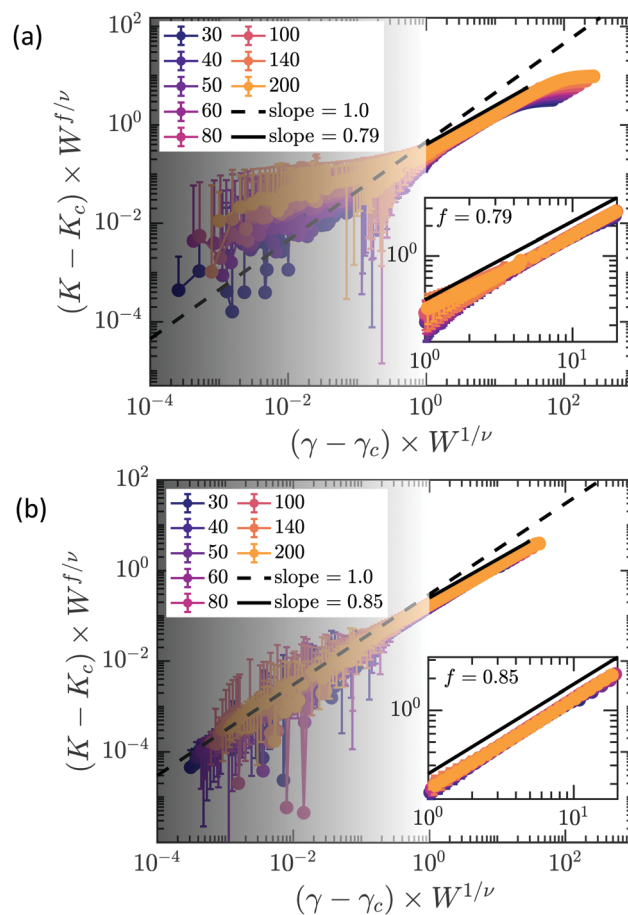
To obtain the stiffness exponent f, we implement a power-law fit of $K - K_c$ *versus* $\gamma - \gamma_c$ for every individual sample of different system sizes in the critical regime, where $|\Delta\gamma| \times W^{1/\nu} > 1$ for every size W. We use sample-dependent K_c and γ_c. Fig. 8a shows the f distributions for different system sizes for a triangular network with $z = 3.3$. The average of these distributions are shown in Fig. 8b. As can be observed, we find negligible differences in f for different system sizes when the exponents are obtained in the true critical regime. However, instead of this size-dependent approach, if the scaling exponents f are collected in a fixed strain window for all sizes, a size-dependent behavior of f is unavoidable due to the finite-size effects (see Fig. S9 in ESI†). We conclude an $f = 0.79 \pm 0.07$ corresponding to $W = 140$ for triangular networks with $z = 3.3$.

By performing an extensive finite-size scaling analysis of the stiffness data for the diluted triangular model in Fig. 9a, we
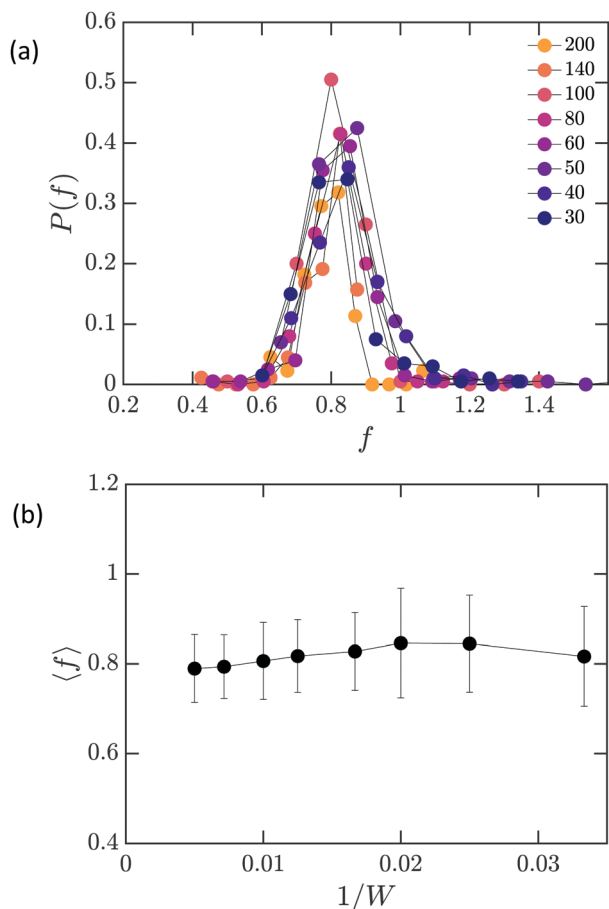
Fig. 8 (a) The distributions of the stiffness exponents f for different system sizes for a triangular network with $z = 3.3$. The exponents are obtained in the critical regime in which $|\Delta\gamma| \times W^{1/\nu} > 1.0$ for all sizes. (b) The ensemble average of f, which is obtained from the distributions in (a), *versus* inverse system size $1/W$. The error bars are showing the standard deviations of samples.

Fig. 9 (a) Finite-size scaling of $K - K_c$ for a triangular network with $z = 3.3$. The inset shows the collapse of data in the critical regime with $f = 0.79 \pm 0.07$. (b) A similar finite-size scaling as in (a) for a 2D jammed-packing-derived model with $z = 3.3$. A distinct analytic regime, *i.e.*, a slope of 1.0 can be observed in this model as $\gamma - \gamma_c \to 0$. The inset, however, shows the non-mean-field exponent $f = 0.85 \pm 0.05$ in the critical regime. The finite-size dominated regime is shaded in both plots.

find three distinct regimes: (i) a finite-size dominated region for $|\Delta\gamma| \times W^{1/\nu} \lesssim 1.0$, (ii) a true critical regime for $1 \lesssim |\Delta\gamma| \times W^{1/\nu}$ and (iii) an eventual large strain regime outside of the critical regime. By using the hyperscaling relation $f = d\nu - 2$, f is the only remaining free parameter used for the analysis in Fig. 9a. As shown in the inset of Fig. 9a, we are able to collapse the data in the critical regime by using $f = 0.79 \pm 0.07$ for a randomly diluted triangular network with $z = 3.3$. A similar finite-size scaling analysis performed for randomly diluted, 2D jammed-packing-derived networks with $z = 3.3$ in Fig. 9b results in a consistent exponent $f = 0.85 \pm 0.05$. In agreement with computational studies in 3D,[20,46] we also find a non-mean-field $f < 1.0$ for 3D jammed-packing-derived networks with $z = 3.3$ (see Fig. S10 in ESI†). This exponent, however, is obtained using only one system size $W = 20$. Further work will be needed for a detailed finite-size scaling analysis in 3D similar to Fig. 9. Nevertheless, prior work has shown a high degree of consistency between the 2D and (the somewhat more limited) 3D simulations. Moreover, experiments on collagen networks have so far shown consistency with 2D models.[20,23] Thus, we have

good reason to believe that our conclusions are not limited to idealized 2D systems.

We note that the exponents we observe are robust to changes or errors in the value of the discontinuity K_c in the critical regime (ii) (see Fig. S11 in ESI†). By performing the same analysis in Fig. 9a, for instance, but using the modulus discontinuity in the thermodynamic limit K_c^∞ instead of sample-dependent K_c, we obtain the same scaling exponent f, provided that $|\Delta\gamma| \times W^{1/\nu} \gtrsim 1$ (see Fig. S12 in ESI†). Thus, we limit our analysis of the critical exponents to the regime (ii) with $|\Delta\gamma| \times W^{1/\nu} \gtrsim 1$, where we find consistent values of $f \simeq 0.79$–0.85, as also reported for Mikado networks previously in ref. 25. These results are, however, inconsistent with ref. 26, where it was argued that $f = 1$ should be generic for fiber networks. We note that it is possible to observe an apparent $f = 1$ regime due to finite size effects, as we clearly observe in Fig. 9b when the system size is smaller than of order $|\Delta\gamma|^{-\nu}$. The apparent exponent f in this case, however, would then not be a critical exponent.[63,67] A natural explanation for an apparent exponent of 1.0 here can simply be

the first term in a scaling function that becomes analytic (and not critical) for a finite system, as has been argued for packings of soft, frictionless particles.[65] We note that the finite-size scaling analysis studied here is a rather general technique for understanding critical phenomena in finite-size computer simulations. Hence, we expect that a similar approach in thermal gel models with intermolecular interactions[68–70] will provide insights about their critical phase transition.

As mentioned before, the sub-isostatic central-force networks can be stabilized by adding bending resistance to fibers. Fig. S13a in ESI† shows the shear modulus *versus* strain for diluted triangular networks with different bending rigidity κ. For such bend-stabilized networks, the shear modulus is captured by the scaling form of eqn (7). To find the exponent ϕ in eqn (7), we fit a power-law to the stiffness data in the regime where $\gamma < \gamma_c$, in which we have $K \approx \kappa |\gamma - \gamma_c|^{f-\phi}$. For individual samples, we find ϕ using the corresponding f exponents that are already collected for central-force networks. For a triangular network with $z = 3.3$, we find $\phi = 2.64 \pm 0.12$ that is obtained by using system size $W = 100$ and $\kappa = 10^{-5}$. The inset of Fig. S13b in ESI† shows the distribution of ϕ. Using these values of f and ϕ, a Widom-like scaling collapse corresponding to eqn (7) is shown in Fig. S13b and c in ESI,† for individual samples and the ensemble average of data respectively.

4 Summary and discussion

In this work, we focus on the critical signatures of mechanical phase transitions in central-force fiber networks as a function of shear strain. As the applied strain approaches a critical value γ_c from above, the stress is borne by a sparse, branch-like structure that is responsible for network stability. By analyzing various moments of the force distributions, we identify scaling exponents for these moments near the transition, similar to prior work on rigidity percolation.[13,50–52] We also find that the fractal dimension of the load-bearing structure at the critical strain appears to be 2.0 in 2D. This is consistent with a finite value of the participation ratio ψ, as well as a finite discontinuity in the network stiffness K in the thermodynamic limit $W \to \infty$.

Further, we study the self-averaging properties of this athermal critical phase transition. We observe a strong self-averaging off criticality, *i.e.*, with relative variance $R_V(X) \sim W^{-d}$ for $X = E$, σ and K. This is consistent with what is expected for thermal systems, based on the Brout argument.[59] At criticality, however, as the correlation length ξ reaches or becomes larger than the system size W, we find a weak self-averaging of all macroscopic properties E, σ, and K at the critical strain. Specifically, $R_V(X) \sim W^{-a}$ with $0 < a < d$. This weak self-averaging at the critical point is in agreement with thermal systems that satisfy the Harris criterion,[58] *i.e.*, for which the heat capacity exponent $\alpha < 0$. As argued in ref. 27, the network stiffness is analogous to heat capacity but with the stiffness exponent $f = -\alpha$. Thus, our observations of weak self-averaging provide further evidence for this analogy and suggest that the

mechanical critical behavior along the line of transitions in Fig. 1 should be insensitive to weak disorder.

By simulating various network models, we confirm that fiber networks exhibit a finite shear modulus discontinuity K_c, in agreement with ref. 25 and 26. We observe a weakly decreasing trend in K_c as a function of system size, but with a non-zero value in the thermodynamic limit. This discontinuity does, however, vanish as the network connectivity z approaches the isostatic point z_c, consistent with ref. 14 and 26. We also find that this discontinuity decreases as one approaches connectivity percolation. We show that allowing for this discontinuity slightly modifies the scaling exponents obtained previously for fiber networks using other methods. The discrepancies between these methods, however, are within the estimated error bars.

Moreover, by repeating the finite-size scaling analysis of the nonaffine fluctuations from ref. 27 we again find evidence for the hyperscaling relation $f = d\nu - 2$[27] and non-mean-field nature of the transition. In estimating the stiffness exponent f, we perform an extensive finite-size scaling analysis that reveals three distinct regimes; besides a critical region with non-mean-field exponents, we find a finite-size dominated region for $|\Delta\gamma| \times W^{1/\nu} < 1.0$, as well as an off critical regime for large strains. In the finite-size dominated regime, we show that the stiffness exponent may appear to be consistent with the mean-field value $f = 1$ (Fig. 9). As noted above, however, this may simply be due to analyticity for finite systems and may have no bearing on possible mean-field behavior. This may explain some reports of mean-field behavior, such as in ref. 26. It is important to emphasize that the scaling exponents cannot be reliably extracted from simulations close to the transition, *i.e.*, for small $|\Delta\gamma| \to 0$, where $|\Delta\gamma| \times W^{1/\nu} \lesssim 1$.

Conflicts of interest

There are no conflicts to declare.

Acknowledgements

References

1 M. F. Thorpe, *J. Non-Cryst. Solids*, 1983, **57**, 355–370.
2 S. Feng, M. F. Thorpe and E. Garboczi, *Phys. Rev. B: Condens. Matter Mater. Phys.*, 1985, **31**, 276–280.
3 D. J. Jacobs and M. F. Thorpe, *Phys. Rev. Lett.*, 1995, **75**, 4051–4054.

4 M. E. Cates, J. P. Wittmer, J.-P. Bouchaud and P. Claudin, *Phys. Rev. Lett.*, 1998, **81**, 1841–1844.

5 A. J. Liu and S. R. Nagel, *Nature*, 1998, **396**, 21–22.

6 M. van Hecke, *J. Phys.: Condens. Matter*, 2010, **22**, 033101.

7 D. Bi, J. Zhang, B. Chakraborty and R. P. Behringer, *Nature*, 2011, **480**, 355–358.

8 D. Bi, S. Henkes, K. E. Daniels and B. Chakraborty, *Annu. Rev. Condens. Matter Phys.*, 2015, **6**, 63–83.

9 J. C. Maxwell, *Trans. – R. Soc. Edinburgh*, 1870, **26**, 1–40.

10 C. R. Calladine, *Int. J. Solids Struct.*, 1978, **14**, 161–172.

11 S. Feng and M. Sahimi, *Phys. Rev. B: Condens. Matter Mater. Phys.*, 1985, **31**, 1671–1673.

12 S. Arbabi and M. Sahimi, *Phys. Rev. B: Condens. Matter Mater. Phys.*, 1988, **38**, 7173–7176.

13 M. Sahimi and S. Arbabi, *Phys. Rev. B: Condens. Matter Mater. Phys.*, 1993, **47**, 703–712.

14 M. Wyart, H. Liang, A. Kabla and L. Mahadevan, *Phys. Rev. Lett.*, 2008, **101**, 215501.

15 C. P. Broedersz, X. Mao, T. C. Lubensky and F. C. MacKintosh, *Nat. Phys.*, 2011, **7**, 983–988.

16 M. Dennison, M. Sheinman, C. Storm and F. C. MacKintosh, *Phys. Rev. Lett.*, 2013, **111**, 095503.

17 M. Dennison, M. Jaspers, P. H. J. Kouwer, C. Storm, A. E. Rowan and F. C. MacKintosh, *Soft Matter*, 2016, **12**, 6995–7004.

18 E. Guyon, S. Roux, A. Hansen, D. Bideau, J. P. Troadec and H. Crapo, *Rep. Prog. Phys.*, 1990, **53**, 373–419.

19 M. Sheinman, C. P. Broedersz and F. C. MacKintosh, *Phys. Rev. E: Stat., Nonlinear, Soft Matter Phys.*, 2012, **85**, 021801.

20 A. Sharma, A. J. Licup, K. A. Jansen, R. Rens, M. Sheinman, G. H. Koenderink and F. C. MacKintosh, *Nat. Phys.*, 2016, **12**, 584.

21 S. B. Lindström, D. A. Vader, A. Kulachenko and D. A. Weitz, *Phys. Rev. E: Stat., Nonlinear, Soft Matter Phys.*, 2010, **82**, 051905.

22 A. J. Licup, S. Münster, A. Sharma, M. Sheinman, L. M. Jawerth, B. Fabry, D. A. Weitz and F. C. MacKintosh, *Proc. Natl. Acad. Sci. U. S. A.*, 2015, **112**, 9573–9578.

23 K. A. Jansen, A. J. Licup, A. Sharma, R. Rens, F. C. MacKintosh and G. H. Koenderink, *Biophys. J.*, 2018, **114**, 2665–2678.

24 F. Burla, S. Dussi, C. Martinez-Torres, J. Tauber, J. van der Gucht and G. H. Koenderink, *Proc. Natl. Acad. Sci. U. S. A.*, 2020, **117**, 8326–8334.

25 M. F. J. Vermeulen, A. Bose, C. Storm and W. G. Ellenbroek, *Phys. Rev. E*, 2017, **96**, 053003.

26 M. Merkel, K. Baumgarten, B. P. Tighe and M. L. Manning, *Proc. Natl. Acad. Sci. U. S. A.*, 2019, **116**, 6560–6568.

27 J. L. Shivers, S. Arzash, A. Sharma and F. C. MacKintosh, *Phys. Rev. Lett.*, 2019, **122**, 188003.

28 B. P. Tighe, J. H. Snoeijer, T. J. H. Vlugt and M. van Hecke, *Soft Matter*, 2010, **6**, 2908.

29 K. Baumgarten and B. P. Tighe, *Phys. Rev. Lett.*, 2018, **120**, 148004.

30 J. L. Shivers, J. Feng, A. Sharma and F. C. MacKintosh, *Soft Matter*, 2019, **15**, 1666–1675.

31 J. Wilhelm and E. Frey, *Phys. Rev. Lett.*, 2003, **91**, 108103.

32 D. A. Head, A. J. Levine and F. C. MacKintosh, *Phys. Rev. Lett.*, 2003, **91**, 108102.

33 C. Heussinger and E. Frey, *Phys. Rev. Lett.*, 2006, **96**, 017802.

34 S. Arzash, J. L. Shivers, A. J. Licup, A. Sharma and F. C. MacKintosh, *Phys. Rev. E*, 2019, **99**, 042412.

35 C. P. Broedersz and F. C. MacKintosh, *Soft Matter*, 2011, **7**, 3186.

36 C. F. Moukarzel, *EPL*, 2012, **97**, 36008.

37 R. Rens, M. Vahabi, A. J. Licup, F. C. MacKintosh and A. Sharma, *J. Phys. Chem. B*, 2016, **120**, 5831–5841.

38 C. S. O'Hern, S. A. Langer, A. J. Liu and S. R. Nagel, *Phys. Rev. Lett.*, 2002, **88**, 075507.

39 C. S. O'Hern, L. E. Silbert, A. J. Liu and S. R. Nagel, *Phys. Rev. E: Stat., Nonlinear, Soft Matter Phys.*, 2003, **68**, 011306.

40 C. P. Goodrich, S. Dagois-Bohy, B. P. Tighe, M. van Hecke, A. J. Liu and S. R. Nagel, *Phys. Rev. E: Stat., Nonlinear, Soft Matter Phys.*, 2014, **90**, 022138.

41 The CGAL Project, CGAL User and Reference Manual, CGAL Editorial Board, 5th edn, 2019.

42 E. Bitzek, P. Koskinen, F. Gähler, M. Moseler and P. Gumbsch, *Phys. Rev. Lett.*, 2006, **97**, 170201.

43 *Numerical recipes in C: the art of scientific computing*, ed. W. H. Press, Cambridge University Press, Cambridge, New York, 2nd edn, 1992.

44 M. Galassi, *et al.*, *GNU Scientific Library Reference Manual*, 2018.

45 A. W. Lees and S. F. Edwards, *J. Phys. C: Solid State Phys.*, 1972, **5**, 1921–1928.

46 A. Sharma, A. J. Licup, R. Rens, M. Vahabi, K. A. Jansen, G. H. Koenderink and F. C. MacKintosh, *Phys. Rev. E*, 2016, **94**, 042407.

47 F. Radjai, M. Jean, J.-J. Moreau and S. Roux, *Phys. Rev. Lett.*, 1996, **77**, 274–277.

48 M. Wyart, *Ann. Phys.*, 2005, **30**, 1–96.

49 T. S. Majmudar and R. P. Behringer, *Nature*, 2005, **435**, 1079–1082.

50 A. Hansen and S. Roux, *J. Stat. Phys.*, 1988, **53**, 759–771.

51 A. Hansen and S. Roux, *Phys. Rev. B: Condens. Matter Mater. Phys.*, 1989, **40**, 749–752.

52 S. Arbabi and M. Sahimi, *Phys. Rev. B: Condens. Matter Mater. Phys.*, 1993, **47**, 695–702.

53 A. Bunde and S. Havlin, *Fractals and disordered systems*, Springer-Verlag Berlin, 1995.

54 K. Bernardet, F. Pázmándi and G. G. Batrouni, *Phys. Rev. Lett.*, 2000, **84**, 4477–4480.

55 P. R. Onck, T. Koeman, T. van Dillen and E. van der Giessen, *Phys. Rev. Lett.*, 2005, **95**, 178102.

56 C. P. Broedersz, PhD thesis, Vrije Universiteit Amsterdam, 2011.

57 R. C. Arevalo, J. S. Urbach and D. L. Blair, *Biophys. J.*, 2010, **99**, L65–L67.

58 A. B. Harris, *J. Phys. C: Solid State Phys.*, 1974, **7**, 1671–1692.

59 R. Brout, *Phys. Rev.*, 1959, **115**, 824–835.

60 S. Wiseman and E. Domany, *Phys. Rev. E: Stat. Phys., Plasmas, Fluids, Relat. Interdisc. Top.*, 1995, **52**, 3469–3484.

61 A. Aharony and A. B. Harris, *Phys. Rev. Lett.*, 1996, **77**, 3700–3703.

62 S. Wiseman and E. Domany, *Phys. Rev. E: Stat. Phys., Plasmas, Fluids, Relat. Interdiscip. Top.*, 1998, **58**, 2938–2951.

63 D. Stauffer and A. Aharony, *Introduction to percolation theory*, Taylor & Francis, London, 2003.

64 A. B. Harris and T. C. Lubensky, *Phys. Rev. B: Condens. Matter Mater. Phys.*, 1987, **35**, 6964–6986.

65 C. P. Goodrich, A. J. Liu and S. R. Nagel, *Phys. Rev. Lett.*, 2012, **109**, 095704.

66 C. P. Goodrich, A. J. Liu and J. P. Sethna, *Proc. Natl. Acad. Sci. U. S. A.*, 2016, **113**, 9745–9750.

67 K. Binder and D. W. Heermann, *Monte Carlo Simulation in Statistical Physics*, Springer Berlin Heidelberg, Berlin, Heidelberg, 2010.

68 O. Peleg, M. Kröger, I. Hecht and Y. Rabin, *EPL*, 2007, **77**, 58007.

69 M. Kröger, O. Peleg, Y. Ding and Y. Rabin, *Soft Matter*, 2008, **4**, 18–28.

70 O. Peleg, M. Kröger and Y. Rabin, *Phys. Rev. E: Stat., Nonlinear, Soft Matter Phys.*, 2009, **79**, 040401.